Assessment of macro and micro mechanical properties of fresh and deteriorated ballast combining laboratory tests and 2D-discrete element methods

Theechalit Binaree, Sararat Kwunjai, Peerapong Jitsangiam, Emilien Azéma, Guoqing Jing

Assessment of Macro and Micro Mechanical Properties of Fresh and Deteriorated Ballast combining Laboratory Tests and 2D-Discrete Element Methods

*[1]Theechalit Binaree , [1]Sararat Kwunjai, [1]*Peerapong Jitsangiam, [2,3]Emilien Azéma, and [4]Guoqing Jing*

[1]Chiang Mai University-Advanced Railway Civil and Foundation Engineering Center (CMU-RailCFC), Department of Civil Engineering, Faculty of Engineering, Chiang Mai University, 239 Huay Kaew Road, Muang, Chiang Mai, 50200, Thailand

[2]LMGC, Université de Montpellier, CNRS, Montpellier, France

[3]Institut Universitaire de France (IUF), Paris, France

[4]School of Civil Engineering, Beijing Jiaotong University, Beijing, 100044, China

**Corresponding author; peerapong@eng.cmu.ac.th*

ABSTRACT

This research initially investigates the mechanical behavior of fresh and fully deteriorated (used) ballast grain assemblies through a combination of laboratory experiments and discrete element modeling (DEM). The extended Los Angeles abrasion (LAA) test generated the used ballast grains at which a fouling index (FI) of 40 %, while fresh ballast grains serve as the reference material. Morphological analysis of angularity properties of fresh and used ballast grains was employed in producing 2D polygonal shapes implemented in a discrete element code. Numerical simulations using the contact dynamics method examined the bi-axial compression of the 2D-equivalent fresh and used ballast grain assemblies under varying confining pressures. Results show that both fresh and used ballast grain packings exhibit similar stress-strain curves, with fresh ballast packing displaying slightly higher shear strength (5%) at the residual state. Fresh ballast packing is denser than the used one at the peak shear state, while residual states show nearly identical volume fractions. Microscale analysis of contact and force networks reveals that the used ballast assembly is more anisotropic in contact at peak stress. At the same time, both packings exhibit similar contact anisotropy at the residual state. Fresh ballast packing exhibits higher force anisotropy, particularly in frictional forces, explaining the excess shear stress observed at the residual state. These findings

suggest that used ballast grains mobilize local friction less efficiently than fresh ballast grains, potentially impacting the lateral strength properties of ballasted tracks. This study provides valuable insights into the behavior of used and fresh ballast grains, serving as a foundation for further investigations.
Keywords; Railway ballast, Ballast fouling, Deteriorated ballast, DEM

1. Introduction

The railway ballast layer is the top of the substructure in a railway track structure system. Its principal function is to provide support and stability for the tracks and distribute the weight of the trains evenly across the tracks [1–3]. When the ballast deteriorates, it can cause problems such as unevenness in the tracks and increased wear on the rails and other components of the track [4,5]. The uneven train loading on the rail track resulted from its irregularities, by which excessive deformation of rail track substructure layers would be the main cause. This result can lead to more frequent maintenance and the more significant use of fresh ballast to repair and maintain the rail track functions. If there is insufficient fresh ballast, properly maintaining the tracks can be questionable, leading to more sourcing of the standard quality rocks to serve such ballasted track maintenance. Reusing deteriorated ballast after its termination for maintenance is an alternative solution to this resource-depleting problem.

It is essential for the ballast used in railway tracks to meet specific performance standards to provide adequate support and stability [6]. Fresh ballast is typically a uniform grade of granular material that is tough enough to resist the impact of traffic loading. It is typically made from hard mineral rock such as granite, basalt, rhyolite, and quartzite that have been crushed to the required particle size. The ballast is typically evaluated based on its physical properties, such as particle size, sharpness, angularity, roundness, surface texture, and mechanical properties, such as abrasion, hardness, and toughness. The traditional methods are used to test the ballast abrasion resistance, which is the ability to withstand wear or erosion due to the passage of trains. Generally, methods, including the Micro-Deval test [7] and the Los Angeles abrasion (LAA) test [8], have been used to evaluate the ballast wearing and abrasive resistance at the laboratory scale. Several ways to simulate ballast deterioration in an experiment depend on the specific factors studied [7,9–11]. Besides, for the in-field conditions, the method for simulating ballast deterioration with

abrasion tests was also utilized, by which a series of study works demonstrated how to simulate the in-field ballast deterioration through the LAA test scheme [12–14]. That helps to understand the factors contributing to ballast degradation and identify potential strategies for improving the performance and service life of the tracks.

The fouling index (FI) is popularly used to express the fouling degree of a ballast layer in a railway track [15]. It is expressed as a percentage (see EQ.1), with a higher value indicating more significant fouling in the ballast layer. The higher the FI, the greater the level of fouling in the ballast bed. The FI can monitor the level of fouling in railway tracks over time and indicate that maintenance may be needed to remove fouled materials with fresh ones. Generally, the 40% FI is used as the threshold for the maximum contamination of a ballasted railway track [15]. After termination, the fully deteriorated ballast or used ballast with a more rounded and less angular shape is disregarded with no more use. Relatively less backup information to encourage reusing such used ballast existed. This study attempted to assess the different mechanical properties of fresh and so-called "used" ballast utilizing the discrete element method (DEM) simulations to promote the first step of the sustainable utilization of the used ballast in the railway sector after termination.

The hardest part of the DEM ballast simulations is forming the ballast particles close to their real morphology characteristics. Some research works relied on simplified models, such as spheres or discs, as ballast particles in the DEM simulations [16–19]. The model simplifies the simulation and reduces the computational demands, as it is generally easier to model spheres or discs than more complex shapes [16,17]. However, it is essential to recognize that these simplified models may not accurately capture the behavior of real ballast particles, which may have more complex shapes and properties. In recent years, some research works have developed sophisticated models to consider more realistic particle shapes [20–23], and along with these modelings, often non-trivial effects have been evidenced. For instance, it is reported non-linear variation of the strength and packing fraction in assemblies when the shape deviates from spherical shape either by increasing grain angularity [24–26], elongation [27,28], or even by modifying the Particle Size Distribution [29–36]. The polyhedral or polygons can help simulate the ballast shape better than the spheres [37–41]. Therefore, the ballast particle model using the polygons can be a helpful starting point for understanding the behavior of ballast grain assembly [39,42], even if it is important to consider the limitations of these models. In the following, the greatest challenge is to

describe the typical shape of fresh/used ballast grains so that they can be implemented in a discrete element code to study the properties of the corresponding assemblies.

The appeal property distinguishing the fresh and used ballast would be the angularity. Angularity refers to the sharpness and irregularity of the edges and corners of the ballast particles. It is also a parameter that describes the shape of individual particles in a soil or rock sample. Typically, it is used to classify rocks based on the degree to which their particles are angular or have sharp edges and corners versus rounded or smoother [43,44]. The angularity can be determined using various methods, such as visual examination, protractor, and digital angle gauge. The most widely used method for finding the angularity of ballast particles is probably visual examination. The ballast particles are examined visually using a magnifying glass or a microscope, and the angularity is estimated based on the appearance of the particles. This method is simple and can be used to quickly get a general idea of the angularity of the ballast. Another widely used method is average angle measurement. The angles of the corners and edges of the ballast particles are measured using a protractor or a digital angle gauge, and the average angle is calculated. This method provides a more accurate and quantitative measure of the angularity of the ballast, but it is more time-consuming and may require specialized equipment. It commonly evaluates ballast particles' angularity by image analysis using image analysis software. It is a quick and accurate method, but it requires specialized software and may not be suitable for all types of ballast grain.

Therefore, the study aims to provide the first step towards a better understanding the rheological properties of assemblies of fresh and used ballast grains by combining experiments and discrete element simulations given a possible reusing of used ballast in the rail track works. The used ballast grains were generated in the laboratory using the LAA test to reach the FI value of 40%. Then, the fresh and used ballast grains were imaged, and a set of polygonal shapes, as a "2D archetypal representation" of the fresh and used ballast grains, were generated considering digital imaging techniques with angularity evaluations. Discrete Element Simulations using these polygonal shapes were conducted under bi-axial loading. This study outputs would elaborate the understanding of the used ballast's macro and micromechanical properties parallel to the fresh ballast under the same loading condition, leading to the forward steps of reusing the so-called used ballast in the maintenance of the ballasted railway track. Evaluating the characteristics of deteriorated ballast for reusing before construction can help ensure the performance and provide

adequate support and stability of ballast for the tracks. However, the current research on recycled ballast is limited, which does not clear the ballast track performance [11,45,46].

2. Experimental methods for generating equivalent 2D grain shapes

To generate 2D polygonal shapes representing fresh and used ballast grains, it is first necessary to define clear and reproducible experimental procedures to discriminate relevant geometrical parameters. This section demonstrates the reference material (fresh ballast grains) that is considered, the method to wear out the ballast grains (LAA test), and the geometrical image analysis strategy to re-construct equivalent polygonal shapes for fresh and used ballast grains.

2.1) Fresh ballast used in this study

The fresh ballast was sourced from only the ballast stockpiles of the Chiang Mai State Railway of Thailand (SRT), Thailand. The deteriorated ballast in this study must be reproduced from the fresh ballast material through the specific milling machine of the LAA tests, the so-called used ballast. All the ballast materials were washed, oven-dried, and cooled at room temperature—then, blending and quartering methods for preparing ballast material before testing. The gradation properties of fresh ballast material used in the laboratory are shown in Fig. 1, which was tested at 100 kilograms per sample. The LAA test was conducted according to ASTM535.

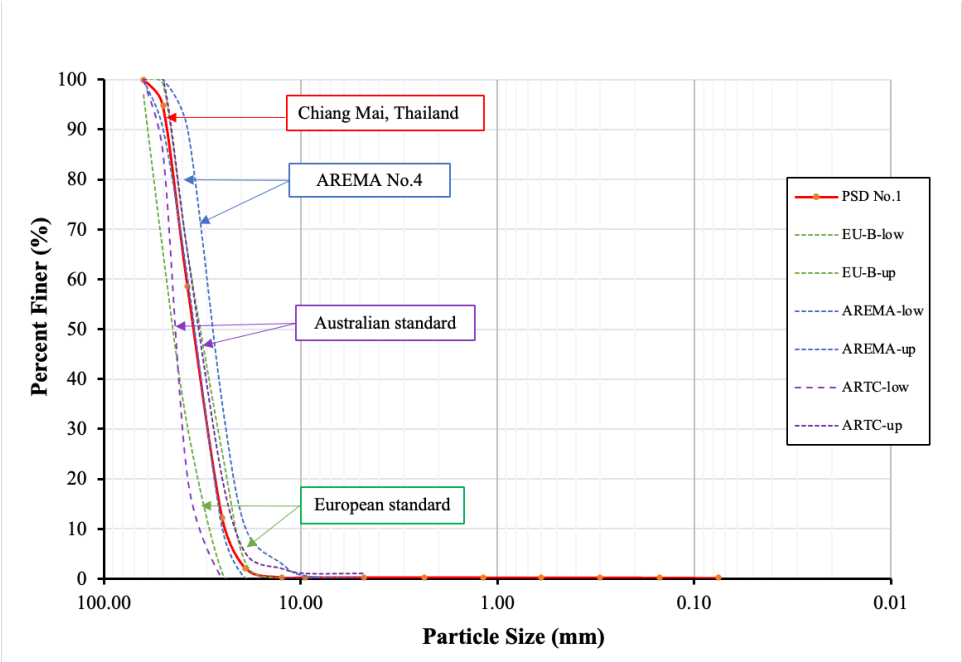

Fig. 1. Gradation of ballast material.

2.2) Generating used ballast through extended LAA test

2.2.1) Brief description of the extended LAA tests:

The LAA test conveys a sample of ballast to wearing and abrasive actions to evaluate its abrasion resistance. The ballast material is placed in a specific rotating drum with steel balls. Typically, the LAA test is a package that only involves a single set of load applications. This study compared the ballast sample to repeated loads over an extended period to reach fine particle generation up to 40% of the FI value. The aggregate sample amount of fresh ballast was 10 kilograms in the LAA milling drum for a fraction of 31.5-50 mm, placing the sample in a rotating drum with 12 steel balls, shown in Fig. 2. After finishing a specific number of LAA tests, sieve analysis was performed to evaluate the ballast material passed the sieve, which measures the fouling index (FI) and particle size distribution (PSD) of ballast material due to abrasion. The FI results were obtained from the sieve analysis after the test carried out trials of specific rounds of LAA. For the particle size analysis, the sample was sieved through a series of sieves with different mesh sizes. The materials passing through each sieve size were collected and weighed. Then, photographs were taken for a particle size and shape analysis procedure that uses imaging

techniques to quantify the particles' size and shape in a ballast sample. This step could provide information about the particle size and shape of the ballast sample, which can be used to evaluate the suitability of the material.

The LAA experiments were repeated until the fouling index value was more than 40 % [15]. A percentage value of more than 40, Selig & Waters (1994) would suggest a relatively high level of fouling in the ballast layer (shown in Fig. 3), which could potentially impact the performance of the tracks. High levels of fouling in the ballast bed can interfere with the ballast's ability to provide adequate support and stability for the tracks. They can also increase the maintenance requirements for the tracks. This method involves collecting a sample of the weighing the materials passing through specific sieve sizes, used to calculate equation 1:

$$\boldsymbol{Fouling\ Index\ (FI) = P_{0.075} + P_{4.75}} \qquad \text{(EQ.1)}$$

where $P_{0.075}$ is the percent passing the No. 200 sieve, $P_{4.75}$ is the percent passing the No. 4 sieve.

Fig. 2. The Los Angeles Abrasion test machine.

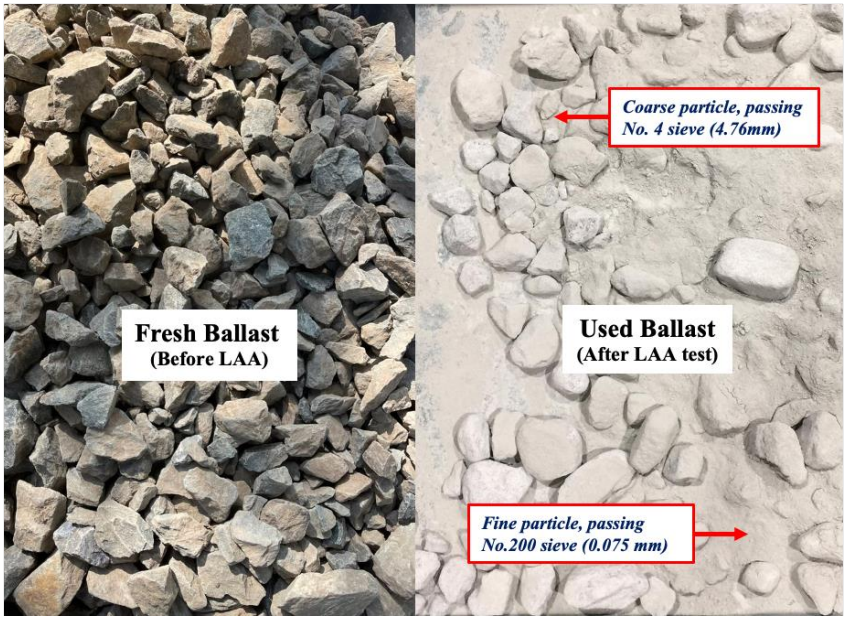

Fig. 3. Changing the fresh ballast to the deteriorated (used) ballast in the laboratory generation.

2.2.2) Particle Size Distribution and grain shapes after the LAA test

Fig 4. gives a general view of the ballast particles grouped by their average size at different levels of the LAA tests (from 0 to 3500 rounds). As the number of LAA rounds increases, the ballast exhibits more wear and abrasion; thus, the proportion of fine particles increases quickly. In contrast, the proportion of the biggest one declines slowly. A similar process may occur on railway tracks by rail traffic loading. This result naturally translates to modifying the particle size distribution (that of the fresh ballasts grain) and increasing the FI index. The relationship between the number of LAA test rounds and the FI may depend on the ballast-specific conditions and the factors contributing to fouling and deterioration. As shown in Fig. 5, the PSD gradually shifts to the right and moves up as the number of rounds of LAA increases with an increase of the FI from 0 to 40. Nevertheless, the general shape of the PSD is maintained even after 3500 rounds. In the following, fine particles (i.e., whose mean diameter is below 9.5mm) are excluded from the analysis.

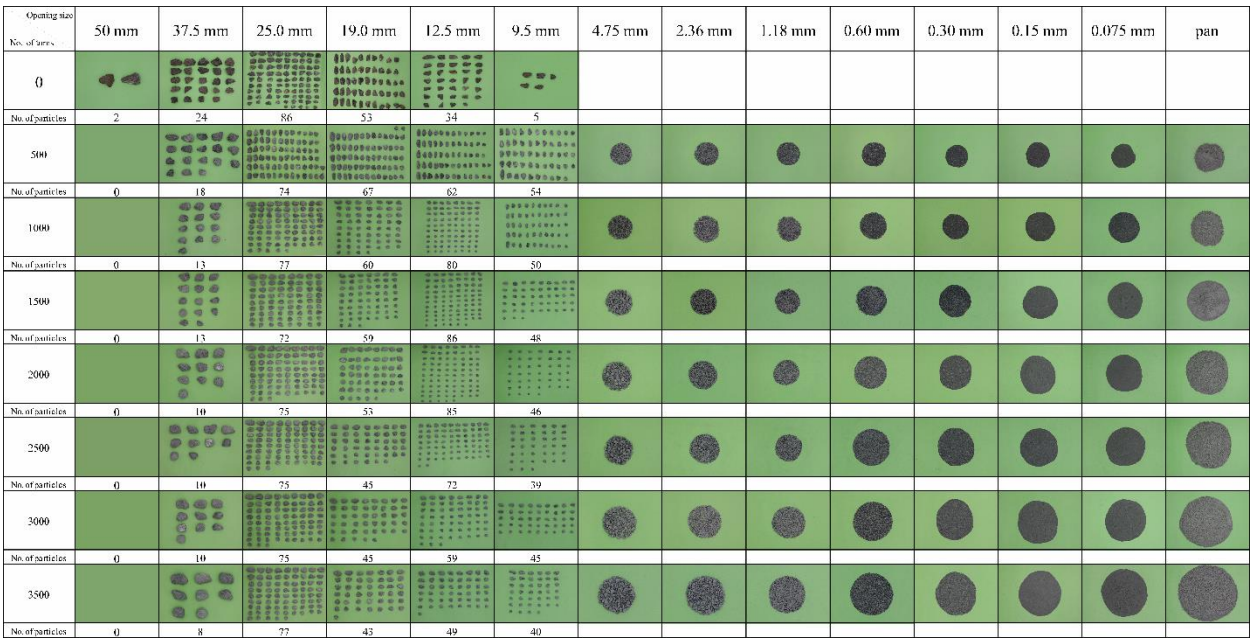

Fig. 4. The visualizations of ballast individual sizes.

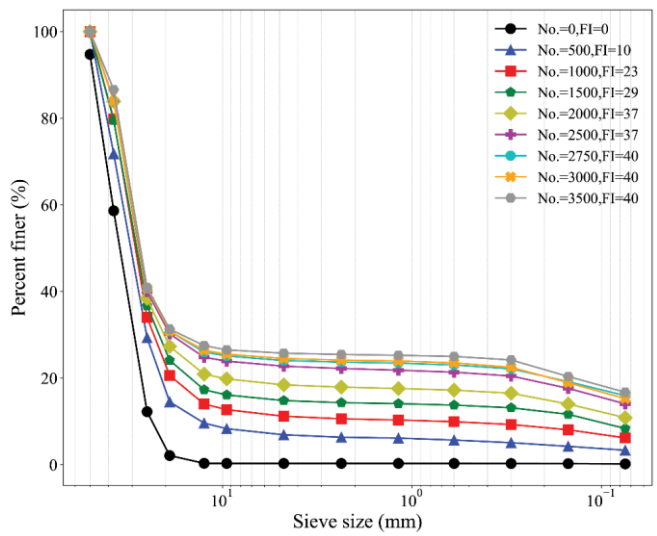

Fig. 5. The gradations curve of repeat LAA rounds.

Along with particle size, Fig. 6 shows a close-up view of the grains for different sizes, both for fresh ballast (a) and used ballast at LAA=3500 (b). Generally, the fresh ballast grains have sharp edges and are slightly elongated in all the granulometric classes considered. On the contrary, the used ballast grains are more rounded and less elongated.

(a)

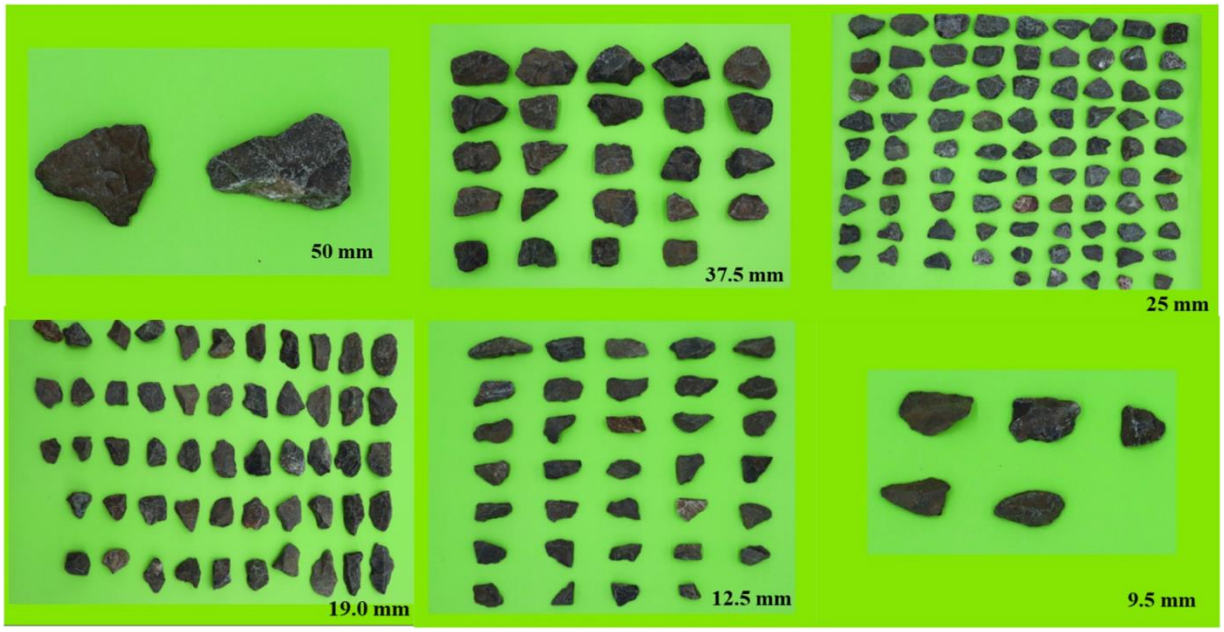

(b)

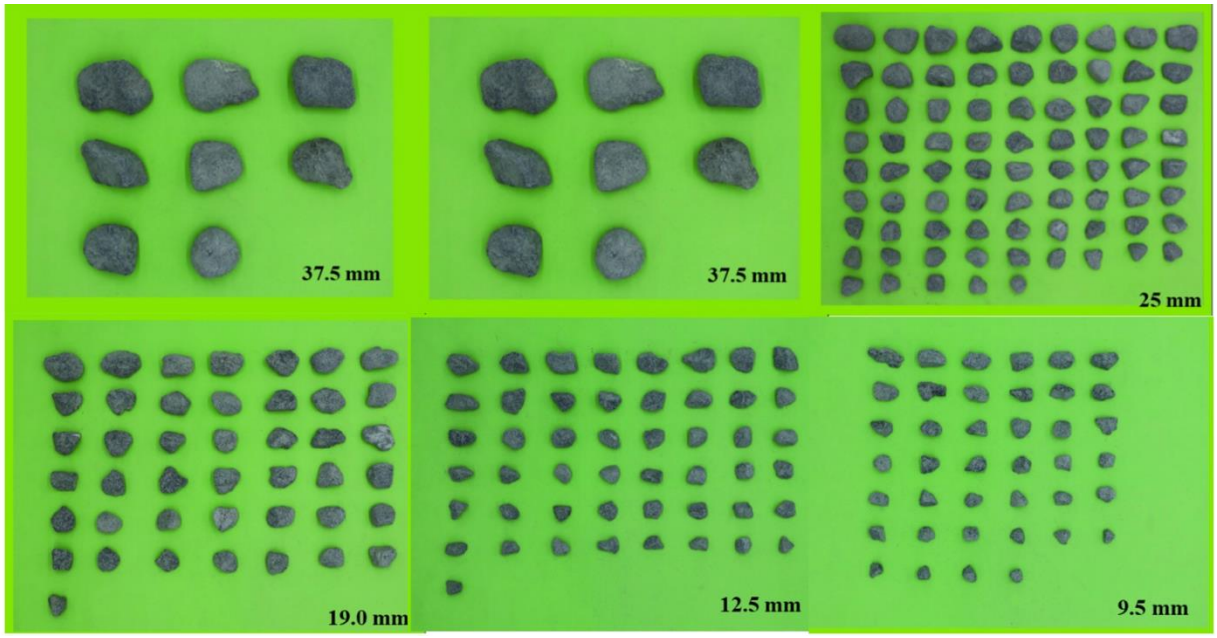

Fig. 6. Close-up view of (a) fresh ballast and (b) used ballast grouped by their mean size.

2.3) Generating representative polygonal shapes for fresh and used ballast by 2D image analysis.

An empirical method is proposed to identify a characteristic polygonal shape of fresh and used ballast grains. Once sorted, the ballast grains are placed on a clean paper surface, and a visual inspection is made to ensure that the grains are of uniform size in each particle size class. 2D photographs of each grain are taken, making sure as much as possible to be positioned parallel to the plane of the laboratory. From the grain images, the "best" enveloping ellipse is constructed for each grain, as illustrated in Fig. 7(a) for fresh ballast and Fig.7(b) for used ballast. The vertices of the grains intercepting the circumscrib ed ellipses are then chosen to generate the 2D-equivalent polygon from the imaged (fresh/used) grain.

However, it should be noted that this method is subjective and depends on the visual evaluation of the grains but potentially also on the person who performs the measurements. Therefore, different operators performed the visual classification of each sample ten times. Several people performed the analysis and compared their results to ensure accuracy. From these empirical analyses, we estimate that one 5-sided polygon, whose shape is shown in the red line in Fig.7a, is representative of fresh ballast. In comparison, one 10-sided polygon shown in Fig.7b represents used ballast. In the following, the two identified polygonal shapes will be used as a proxy for fresh and used grains and implemented in a discrete element code.

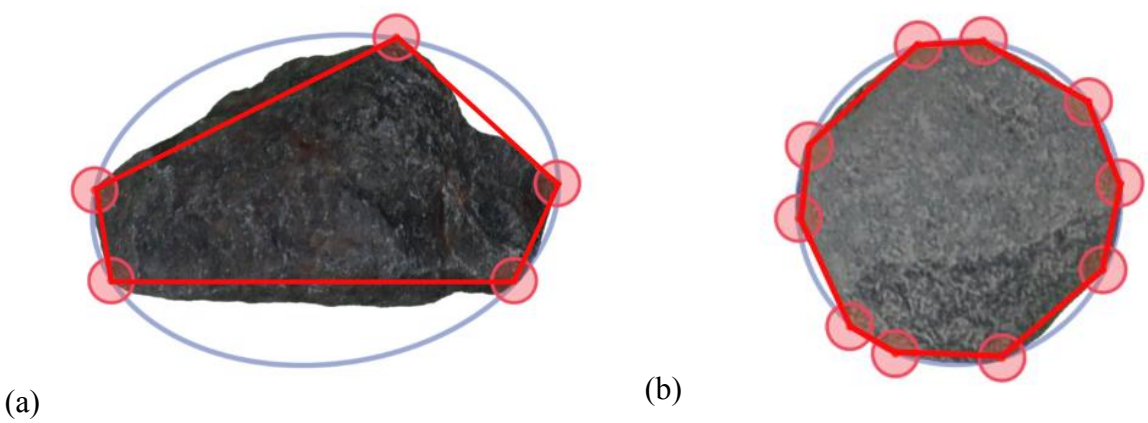

Fig. 7. Generic polygons (red line) representing fresh (a) and used (b) ballast grain constructed from imaged real grains.

3. Numerical procedures

3.1) Simulation method.

The simulations use the Contact Dynamics (CD) method with irregular polygonal particles. The CD is a discrete element approach, originally developed by J.-J.-Moreau and M. Jean [38,41,47,48], based on an implicit time integration of the equations of motion and non-regularized contact laws. In other words, no elastic repulsive potential and no smoothing of the Coulomb friction law for the determination of forces are used, contrary to the "Soft-Sphere-DEM (SSDEM)" (or Molecular Dynamic-like) approach originally developed by Cundall [49]. Thus, contact interactions and Coulomb friction law are treated as complementarity relations in CD. The equations of motion for each particle are formulated as differential inclusions in which velocity jumps replace accelerations. Therefore, the parameters to consider in the CD approach are a dry friction coefficient μ_s and two restitution coefficients (normal and tangential), which control the amount of energy dissipated during collisions. The unknown variables (i.e., particle velocities and contact forces) are simultaneously solved via a non-linear iterative Gauss-Seidel scheme. Hence, the CD method is numerically stable, and the simulations can be performed with large time steps compared to SSDEM. For more details related to the mathematical formulation of the CD, see Refs. [48,50].

Modeling irregular polygonal particles in the frame of the CD method is straightforward since a side-vertex ("sv") or a side-side ("ss") contact can be represented by only 1 or 2 points, respectively, as illustrated in Fig. 8. For sv-contacts the normal vector is defined perpendicular to the side. For ss-contacts, two points along the sides that come into contact are considered (i.e., the points at the ends of the contact segment), and the normal vector is perpendicular to these common sides. In numerical terms, this entails calculating two forces, but in practice, only their resultant force and the point of application are physically relevant. Finally, vertex-to-vertex ("vv") contacts, although very rare, may also occur. In this case, vv-contacts are treated as ss- or sv-contact based on the path the two particles follow. A comprehensive explanation of the CD method, including the specific handling of contacts between polygonal particles, can be found with details in Ref [24]. The open-source platform LMGC90, developed by the University of Montpellier in France, was used for our research [42,51]. Based on the CD method, this platform is widely used in the

field of granular materials simulation, both in two and three dimensions with grains of various shapes [27,34,37,39,52] and sizes [26,31–33].

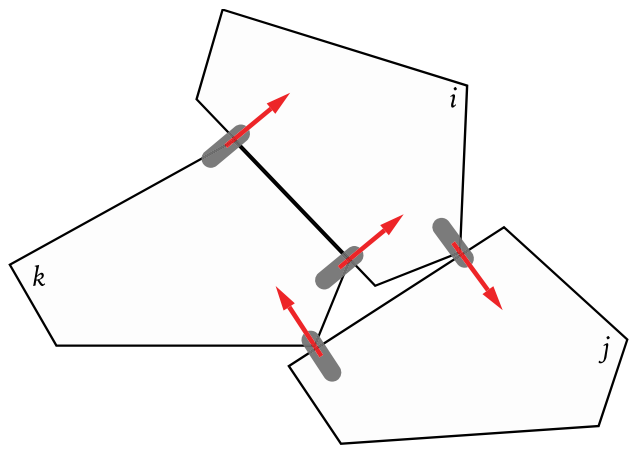

Fig. 8. Schematic representation of contacts between polygonal particles (2D-equivalent fresh ballast in this example): side-to-vertex (*s*v) contacts between the particle *{k,i} and {i,j}*, and side-to-side (*ss*) contact between the particle *k* and *i*. The red arrows represent the unit normal vector.

3.2) Packing construction and bi-axial simulations.

Two numerical samples, both made of 10,000 irregular polygons with a particle size distribution (defined from the circumscribed circles of polygons) uniformly varied between 10mm and 40 mm by volume fraction, were generated. The first sample, called S1, is composed of 5-sided polygons whose generic shape is shown in Fig.7a and accounts for fresh ballast grain assembly. The second sample, S2, comprises irregular 10-sided polygons whose generic shape is shown in Fig.7b and accounts for used ballast grain assembly. Based on the variability of the irregularity of the shapes (resulting from the statistical experimental identification of the equivalent 2D polygonal shape for fresh/used ballast), the angular positions of the vertices are also slightly randomly perturbated around their referential position by an angle of 15degre.

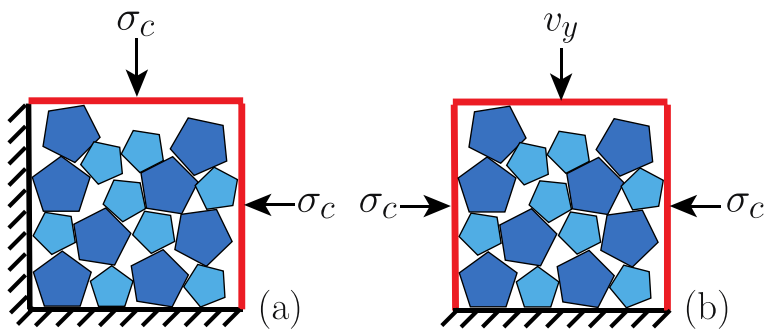

Fig. 9. The sample diagram: (a) Isotropic compression and (b) biaxial shearing test.

Both samples were prepared according to the same protocol. First, a dense packing is constructed using a layer-by-layer deposition model based on simple geometrical rules [53]. The samples are then compressed isotropically under constant stress $\sigma_c = 10\ kPa$ applied to the top and to the right walls, while the left and bottom walls remained fixed; see Fig. 9(a). The gravity and the coefficient of friction between grains and with the wall were set to zero to avoid force gradients in the samples during the isotropic compression. Fig. 10. displays particle-scale views of the two packings at the end of isotropic compaction. Then, the grain-grain friction is set to 0.4, and the isotropically prepared packing where biaxially sheared by imposing a vertical velocity, v_y , on the upper wall while maintaining a constant confining stress σ_c on the lateral walls; see Fig. 9(b). Three confining stresses are tested with σ_c equal to 20 kPa, 40 kPa, and 60 kPa. It is to ensure that all systems remain in the quasi-static state (i.e., rate-independent), the imposed velocity is chosen, such as the Inertial Number I [54], defined by $I = \dot{\varepsilon}\sqrt{\mathrm{m}/\sigma_\mathrm{c}}$, where $\dot{\epsilon} = v_y/H_0$ with H_0 is the sample height at the beginning of bi-axial test and m is the particle mass, is well below 1 for all tests. In all our bi-axial simulations, I is fixed to 10^{-4}.

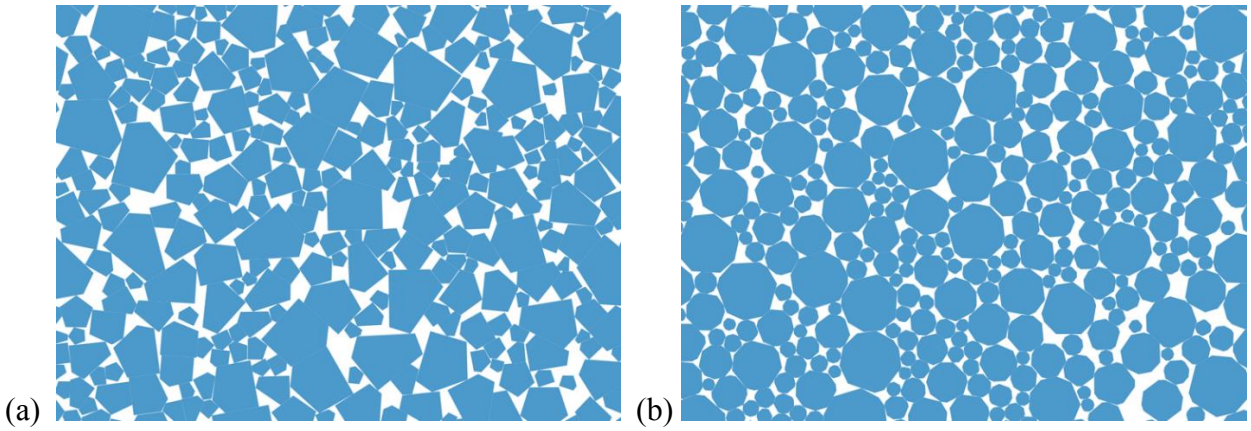

Fig. 10. Particle-scale view of the packing S1(a) and S2(b) that account for a 2D equivalent representation of fresh ballast and used ballast assembly, respectively.

4. Numerical results

4.1) Macroscopic behavior.

This section discusses the stress-strain properties and volume change behavior between the packing of fresh ballast grains (S1) and used ballast grains (S2). Assuming that the granular assembly obeys the Mohr-Coulomb criterium, the strength of the material can be expressed in terms of the internal macroscopic friction φ, which is defined as $sin\,\varphi = q/p$ [44,55], being the deviatoric stress $q = (\sigma_1 - \sigma_2)/2$ and the mean pressure $p = (\sigma_1 + \sigma_2)/2$ for 2D biaxial geometry. The principal stresses σ_1 and σ_2 are computed at any stage of the deformation via the granular stress tensor defined as [56,57]:

$$\sigma_{ij} = \frac{1}{V}\sum_{c\in V} f_i^c l_j^c, \qquad \text{EQ. 2}$$

Where, ℓ_j^c is the j component of the vector joining the centers of the two touching particles at contact c, f_i^c is the i component of the force vector at contact c, and V is the total volume. The vertical strain parameter is given by $\varepsilon_1 = \Delta H/H_0$, with $\Delta H = H - H_0$, where H is the height of the assembly. Finally, the packing fraction is given by the ratio $\rho = V_p/V$, with V_p the volume occupied by the particles.

Fig. 11 shows the evolution of the stress ratio q/p (a) and the solid fraction ρ (b) in S1 and S2, as a function of the vertical strain ε_1, and for different values of the confining stress σ_c. A

classical response for both packings (S1 and S2) is obtained. Regardless of the confining stress values, a stress peak is observed around 2% of deformation, followed by a softening phase before reaching a stress plateau for $\varepsilon_1 > 12\%$ indicating a steady state, also called "residual state" in soil mechanics [44], is reached. In this residual state, the shear strength fluctuates around a mean value. It should be noted that the peak stress is close between the two systems, while the residual shear stress is slightly higher in S1 (i.e., for the 2D equivalent fresh ballast grain packing) than in S2 (i.e., the 2D equivalent used ballast grain packing). At the same time, all packing dilates during the deformation. This translate by a rapid decrease of ρ, until a nearly constant volume is obtained precisely for $\varepsilon_1 > 12\%$, both in S1 and S2, and for all confining pressures. Interestingly, up to small fluctuations, all samples seem to converge towards the same level of packing fraction in the residual state. In the following, the data will be averaged over the steady state whenever the residual state is mentioned.

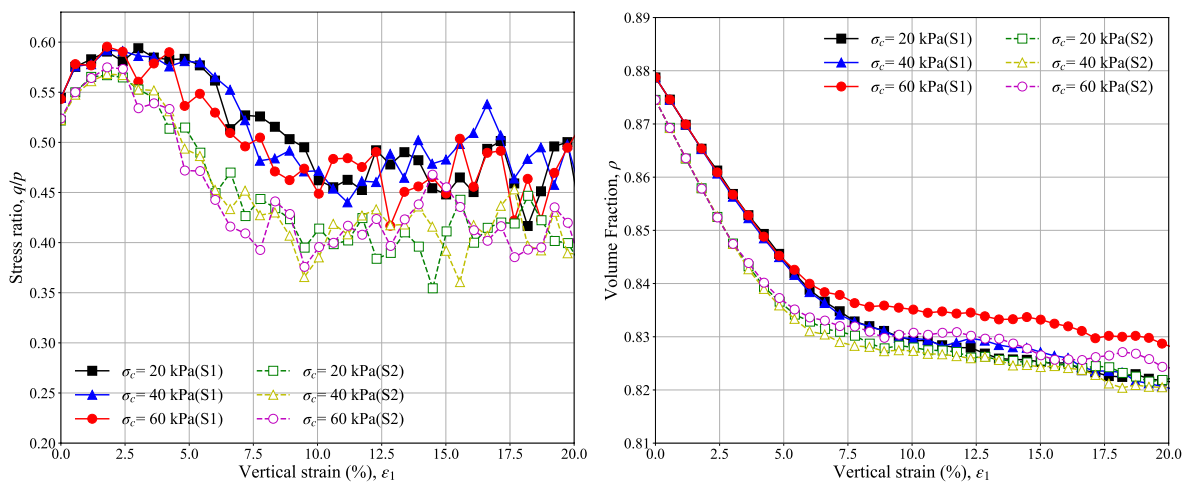

(a) (b)

Fig. 11. Stress-ratio q/p (a) and solid fraction ρ (b) as a function of the vertical strain ε_1 and for different values of the confining stress σ_c, in S1 (full symbol/solid line) and S2 (empty symbol/dashed line).

The corresponding Mohr-Coulomb envelops, plotted in the $(p - q)$ Planes are shown in Fig. 12, both at the peak and residual state in S1 and S2. First, it could be seen that our data are well approximated by straight lines, as defined by the Mohr–Coulomb criterion. Second, we can estimate the internal macroscopic friction angle value for the 2D-equivalent fresh and used ballast

grain packings. We get $\varphi_{S1}^{peak} \simeq \varphi_{S2}^{peak} \simeq 0.58$, where φ_{S1}^{peak} and φ_{S2}^{peak} are the values of the internal macroscopic friction angle at the peak state for S1, S2, respectively. In contrast, we get $\varphi_{S1}^{*} > \varphi_{S2}^{*}$, with $\varphi_{S1}^{*} = 0.47$ and $\varphi_{S2}^{*} = 0.41$ the internal macroscopic friction angle at the residual state for S1, S2, respectively. Therefore, our data suggest that, although fresh and used ballast grain packings exhibit similar values of the residual-state packing fraction $\rho^{*} \sim 0.825$, fresh ballast grain packing has a slightly larger residual state macroscopic friction angle than used.

To better understand the reasons behind higher residual strength values in fresh ballast grain assemblies than in used ballast grain assemblies, we focus on microscopic properties such as grain connectivity and force and fabric networks in the following section.

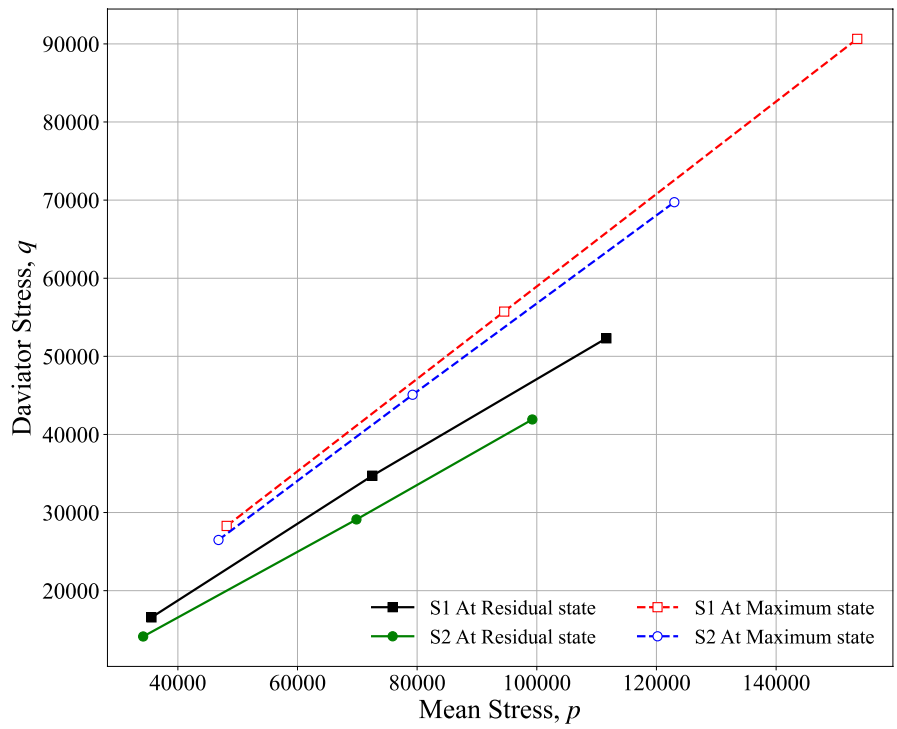

Fig. 12. Mohr-Coulomb failure envelopes obtained for the 2D equivalent fresh (S1) and used (S2) ballast in the (p,q) plane, both at the peak (empty symbol/dashed lines) and residual (full symbols/lines) state.

4.2) Micromechanical description.

When discussing granular microstructure, it is customary to refer to how particles, contacts, and forces organize themselves in space. This organization is governed by factors like steric exclusions (i.e., the volume occupied by the particles) and force equilibrium conditions, which depend on the specificities of the particles' shape and size.

For example, Fig. 13 shows a particle-scale view of the contact network in S1 (a) and S2 (b), both in the residual state. Contacts are visually represented as lines connecting the contact points to the center of the particles. Grains with either zero or one contact, commonly referred to as "floating particles, " are depicted in light grey. In general terms, the contact network topology varies between fresh and used ballast grain packings. In S2, the floating particles tend to be grouped, whereas, in S1, they are, on average, isolated.

Conversely, the contact network appears to exhibit greater connectivity in S1 than in S2 since particles with sharp corners (as in S1) can establish deeper contact with their neighboring particles in contrast to the more rounded particles within S2. Along with contacts, Fig. 13 (c) and (d) shows a particle-scale view of the residual state of the force network within both assemblies. As classically done for such visualization, line thickness is proportional to the normal force magnitude. Visual inspection reveals that, on average, long force chains are mainly oriented vertically (from the top wall to the bottom wall of the packings), emphasizing the compression direction (vertical) and the anisotropic nature of the force network. Moreover, the chains of forces seem stronger but more tortuous in the S1 assembly than in S2.

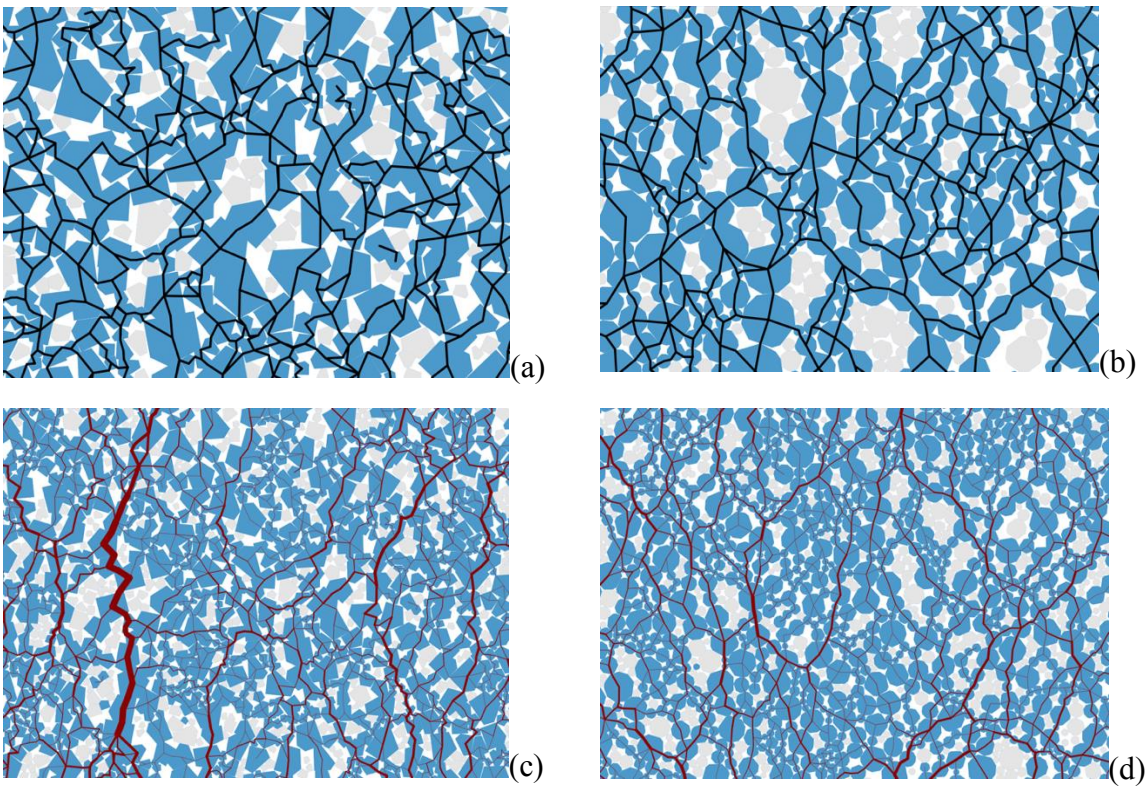

Fig. 13. Close-up view of contact network for fresh (a) and used ballast (b) packing and force network for fresh (c) and used ballast packing (d) in the residual state.

4.2.1) Particle connectivity.

The connectivity of the assemblies can be described by the coordination number Z defined as the mean number of contacts per non-floating particle. It should be noted that floating particles, representing 28.5% of the particles in S1 and 31.2% in S2, are removed from the analysis. Note also that ss-contacts are counted only once, although numerically they represent two geometrical contacts as discussed in Sec. III.1. Figure 14(a) displays the evolution of Z as a function of the vertical strain ε_1, and for different values of the confining stress σ_c, both for S1 and S2. The coordination number decreases rapidly during the deformation toward a steady state value in the residual state, which is slightly higher for S1 ($Z \sim 3.2$) than for S2 ($Z \sim 3.05$) and which is independent with σ_c. It should be noted that this difference is quite small in comparison to the initial configuration, where both systems are prepared within the same condition ($Z_0 \sim 3.6$ for S1 and $Z_0 \sim 3.3$ for S2).

Further inside, the connectivity of the particle can be described using the fraction $P_c(c)$ of particles having exactly c contacts. Figure 14(b) shows $P_c(c)$ in the residual state and at the peak state (inset) both for S1 and S2 (recalling that particles with 0 or 1 contact are removed from the statistics). All plots are nearly similar, with a marked peak at c=3. In both samples, the proportion of particles with two contacts is larger than that of particles with 4 and 5 contacts. Nevertheless, P_4 and P_5 are slightly larger in S1 than S2, while P2 is higher in S2 than S1. This finding explains the higher value of Z in fresh ballast than in used ballast. Indeed, since (by definition) $Z = \sum_{c=2}^{\infty} cP_c(c)$, the fresh ballast assembly is better connected than the used ballast assembly mainly because of a larger proportion of particles with more than four contacts.

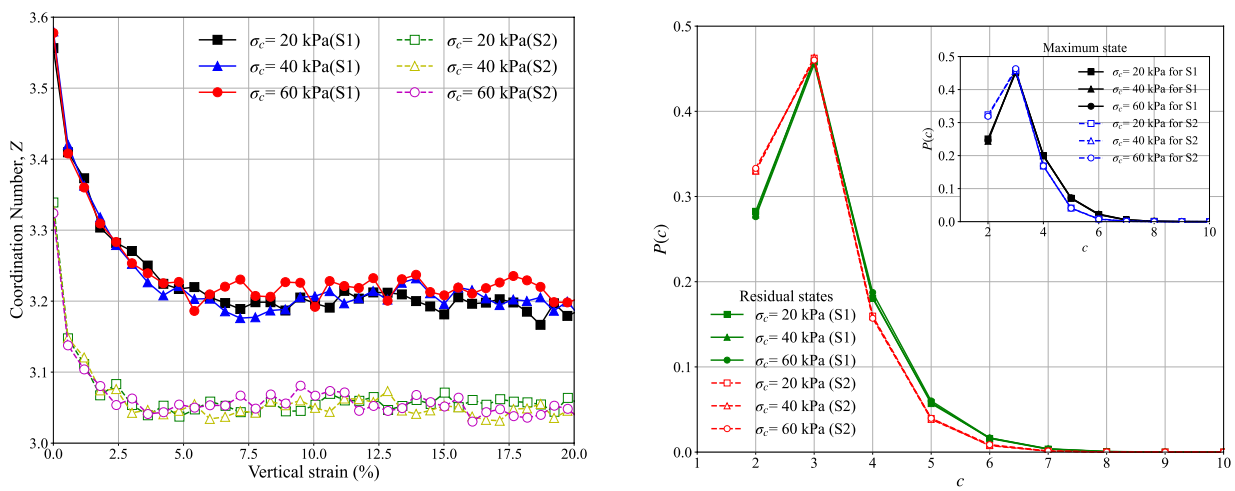

(a) (b)

Fig. 14. (a) The coordination number Z as a function of the vertical strain ε_1 and for different values of the confining stress σ_c, in S1 (full symbol/solid line) and S2 (empty symbol/dashed line). (b) Connectivity $P_c(c)$ of particles, defined as the proportion of particles with c contacts, both for S1 (full symbols/lines) and S2 (empty symbol/dashed lines) in the residual state (the inset show $P_c(c)$ at the peak state).

4.2.2) Anisotropic nature of the contact and force network

The previous description in terms of particle connectivity gives a first picture of the effect of the nature of the ballast grains, i.e., fresh *vs* used, on the microstructure of the assemblies. Nevertheless, the differences in Z and P_c values between fresh and used ballast are small. They

cannot explain the observed differences in macroscopic resistance between the two types of ballast packings. The coordination number Z, and the probabilities $P_c(c)$, as a scalar number, are not sufficient to describe the anisotropic nature of the contact and force network as depicted in Fig.14. As suggested by Eq. 2 (from which the macroscopic shear strength is computed), more quantitative and precise descriptions can be obtained from the densities of contacts and forces according to the contact orientation defined from the unit contact normal vector, $\vec{n}$ [27,57].

In what follows, we adopt the "stress-force-fabric (SSF)" approach, originally developed by Rothenburg and Bathurst [57], which links the anisotropic nature of contact and force networks to the macroscopic shear strength. In 2D, the unit contacts the normal vector, $\vec{n}$,is described by a single angle θ. Thus, the probability density function $P(\theta)$ of contact orientation, θ gives the necessary statistical information about the contact network. Considering also that the contact force vector $\overrightarrow{f^c}$, at a contact c, can be split in terms of its normal (f_n^c) and tangential (f_t^c) component as $\overrightarrow{f^c} = f_n^c\overrightarrow{n^c} + f_t^c\overrightarrow{t^c}$, with $(\overrightarrow{n^c}, \overrightarrow{t^c})$ the local contact frame, the force network anisotropy can be deeper characterized by the mean normal force orientation $\langle f_n\rangle(\theta)$ and the mean tangential force orientation $\langle f_t\rangle(\theta)$ as a function of contact orientation θ. As shown in several previous studies, the three distributions $P(\theta)$, $\langle f_n\rangle(\theta)$ and $\langle f_t\rangle(\theta)$ encapsulates the mains details of the contact network and force transmission resulting from grains properties in granular systems. The polar representation of these functions is shown in Fig. 15, both for fresh (black dot) and used (red dot) ballast in the residual state. As classically observed for bi-axial shearing, the distributions adopted a π-periodic anisotropic shape with a marked peak along the compression axis for $P(\theta)$ and $\langle f_n\rangle(\theta)$, while the maximum is reached around $\theta \sim \pi/4$ for the mean tangential force orientation. The interesting features of such distributions is that, since their overall shapes are quite simple, a first order Fourrier expansion is sufficient to capture their main characteristics as [24,28,31,57]:

$$P(\theta) = \frac{1}{2\pi}[1 + a_c \cos 2\,(\theta - \theta_\sigma)]$$
$$\langle f_n\rangle(\theta) = \langle f_n\rangle[1 + a_n \cos 2(\theta - \theta_\sigma)] \qquad \text{Eq.3,}$$
$$\langle f_t\rangle(\theta) = -\langle f_n\rangle a_t \sin 2(\theta - \theta_\sigma)$$

Where a_c is the contact anisotropy parameters, a_n the normal force anisotropy parameter, a_t the friction force anisotropy parameters and $\theta_\sigma \simeq \pi/2$ the principal stress direction in bi-axial geometry.

As shown in Fig. 15, the above functions nicely approximate the distributions. Finally, it can be shown that after some mathematical manipulations/simplifications in which Eq.3 is implemented in the integral form of Eq.2, the anisotropic parameters add together to build the macroscopic shear strength by [27,57]:

$$\frac{q}{p} \simeq \frac{1}{2}(a_c + a_n + a_t) \qquad \text{Eq.4}$$

As illustrated in Fig. 16(a), the approximation of q/p given by Eq.4 perfectly fit with its direct measurement all along the deformation (shown here only for $\sigma_c = 20\ kPa$ for the sake of clarity). Thus, Eq.4 evidence that the anisotropic parameters, as defined above, are the key descriptors of the microstructure. Note that Eq.4 could be completed considering the branch length anisotropy computed from the mean angular distribution of the branch vector $\vec{l}$. But in the weakly polydisperse system, this anisotropy remains near zero [34–36].

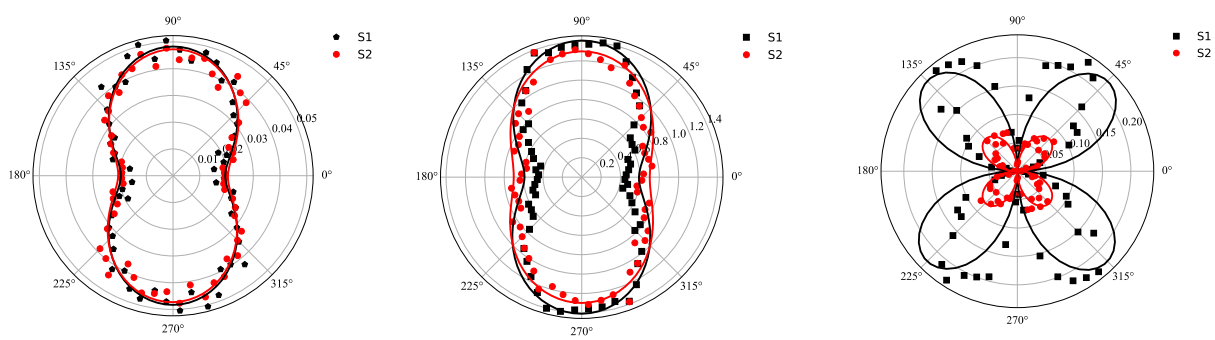

Fig. 15. Polar representation of the probability density function $P(\theta)$, $\langle f_n \rangle(\theta)$ and $\langle f_t \rangle(\theta)$ in the residual state both for fresh (black symbols) and used (red symbols) ballast. The full lines show the approximations given by Eq3.

The evolution of the three anisotropic parameters as a function of the vertical deformation is shown in Fig.16(b), both for S1 (fresh ballast, full lines) and for S2 (used ballast, dashed lines). Generally, the normal and friction forces anisotropies are higher in fresh ballast packing than in used ballast packing all along the deformation. On the other hand, contact anisotropy is initially higher in used ballast packing than in fresh ballast packing, especially at the peak state. But interestingly, geometric anisotropy decreases after the peak state in the used ballast, so both systems have the same level of geometric anisotropy in the residual state.

Thus, under Eq.4, it can be argued that the peak stress in used ballast grains packings mainly results from geometrical anisotropy. In contrast, the peak stress is enhanced by force anisotropies in fresh ballast grain packing which compensates for the lower value of the contact anisotropy and explains the closer values of the peak shear stress. On the same idea, the higher value of the residual shear strength in S1 is mainly due to force anisotropies since geometrical anisotropies are similar in both systems. In particular, noting that the friction force anisotropy is linked to the mean contact friction mobilization between grains ($a_t \propto \langle f_n \rangle / \langle |f_t| \rangle$) [25,27], the higher value of a_t in S1 indicates a higher proportion of particles tend to slide than rolling in fresh ballast grain assembly, than in used ballast grain assembly. In other words, friction mobilization is one of the key mechanisms developed for fresh ballast grains. From a railway application perspective, this result suggests that fresh ballast grains would provide better lateral resistance for the ballasted track than used ballast grains.

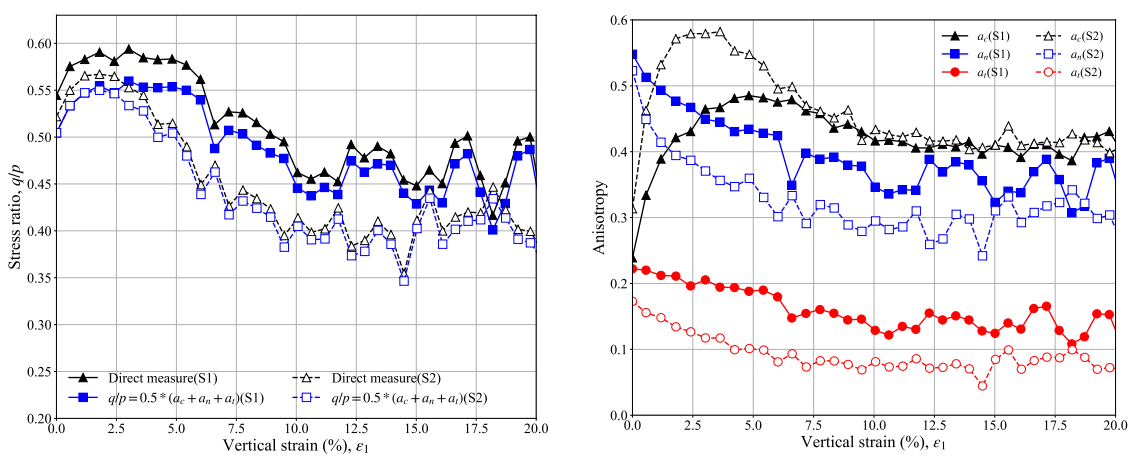

(a) (b)

Fig. 16. Evolution of the normalized shear strength q/p as a function of the vertical deformation ε_1 for fresh (S1-full line) and used (S2-dashed line) ballast grain assembly at $\sigma_c = 20\ kPa$ (the same as in Fig. 11(a)), together with the approximation given by Eq.4 (full symbols for S1, empty symbol for S2). (b) Evolution of anisotropic parameters as of function of the vertical deformation ε_1 for fresh (S1-full line/full symbols) and used (S2-dashed line/empty symbol) ballast grain assembly at $\sigma_c = 20\ kPa$.

5. Concluding remarks and recommendations

The general aim of this study was to numerically investigate the mechanical behavior of fresh and used ballast grain packings under the bi-axial applied loading conditions, both at the macro and micro scale, employing simplified bi-dimensional DEM. For this purpose, one of the challenging issues was to define archetypal grain shapes that reflect the fresh or used character of ballast grains in a simple but sufficiently representative way.

First, an empirical and extensive experimental campaign was carried out to identify the 2D-equivalent shapes of fresh and used ballast grains utilizing bi-dimensional image analysis. It extended the Los Angeles abrasion (LAA) test to wear the grains. This experimental study showed that fresh ballast grains can be approximated by a 5-sided, slightly elongated polygonal shape. On the other hand, it is shown that the shape of used ballast grains is better approximated by a 10-sided, rather rounded, polygonal shape.

Secondly, the archetypal fresh and used ballast grain shapes identified experimentally were implemented in a discrete-element code based on the Contact Dynamics approach. Large assemblies composed of the 2D-equivalent fresh and used grains have been systematically sheared in a bi-axial configuration for different confining pressure.

As a general observation, both fresh and used ballast grain packing exhibit similar stress-strain behavior with a marked peak stress followed by a softening phase and a constant stress plateau in the residual state. Interestingly, the packing of 2D-equivalent fresh and used ballast grains are relatively close in peak shear stress. Still, the residual shear stress is slightly higher (around 5% of difference) for the fresh ballast grain packing than for the used ballast grain packing, suggesting that used and fresh ballast grains offer similar normal stress resistance in the ballasted track

geometry. Nevertheless, a detailed microstructure analysis regarding particle connectivity and anisotropy of the contact and force network reveals that fresh ballast grains better mobilize the local friction than used ballast grains. As a result, force chains are better stabilized, leading to higher normal and force anisotropy values. In other words, and from a practical point of view, these findings suggest that fresh ballast grains would provide better lateral resistance for the ballasted track than used ballast grains. Based on the observations of the capability of withstanding the vertical and lateral movements of the fresh and used ballast packings, it would be shed a light to reuse the so-called used ballast in the railway track application by discovering some method to increase the lateral deformation resistance because of the vertical deformation of both material exhibits almost equally.

Finally, it should be noted that awareness would be raised that the work presented here, like all 2D works, is essentially qualitative. However, the highlighted macroscopic trends and the microscopic mechanisms provide a clear roadmap for future extensive three-dimensional studies, where ballast grains would be simulated by more realistic polyhedral shapes [58,59]. Nevertheless, some questions that can be systematically explored through 2D and 3D simulations remain. For instance, how can we reuse the used ballast effectively? Can we mix the used ballast with the fresh ballast? Other issues concern the possible size effects inherent in the ballasted track structure. Indeed, greater behavioral variability can be expected with fewer grains. How these variabilities evolve as a function of ballast layer thickness with fresh, used, or a mixture of fresh/used ballast grain is a question to be addressed.

6. Acknowledgements

The authors would like to extend their gratitude and acknowledge Chiang Mai University through the research and innovation research support scheme of Fundamental Funds (FF65/080) for the financial support and the University of Montpellier for the LMGC90 program and its associated facility support. The first author would also thank Chiang Mai University for supporting the postdoctoral scholarship-2022.

7. References

[1] Das BM. Geotechnical engineering handbook. J. Ross publishing; 2011.

[2] Indraratna B, Ngo T. Ballast railroad design: smart-uow approach. CRC Press; 2018.

[3] Li D, Hyslip J, Sussmann T, Chrismer S. Railway geotechnics. CRC Press; 2015.

[4] Rosa AF, Aragão FTS, da Motta LMG. Effects of particle size distribution and lithology on the resistance to breakage of ballast materials. Construction and Building Materials 2021;267:121015.

[5] Tutumluer E, Schmidt S, Qamhia I, Basye C, Li D, Douglas S. Ballast properties and degradation trends affecting strength, deformation and in-track performance. Proceedings of the AREMA 2015 Annual Conference in conjunction with the Railway Interchange, Minneapolis, MN, 2015.

[6] Kruglikov A, Yavna V, Ermolov Y, Kochur A, Khakiev Z. Strengthening of the railway ballast section shoulder with two-component polymeric binders. Transportation Geotechnics 2017;11:133–43.

[7] Gökalp İ, Uz VE, Saltan M. Testing the abrasion resistance of aggregates including by-products by using Micro Deval apparatus with different standard test methods. Construction and Building Materials 2016;123:1–7.

[8] Guo Y, Markine V, Qiang W, Zhang H, Jing G. Effects of crumb rubber size and percentage on degradation reduction of railway ballast. Construction and Building Materials 2019;212:210–24.

[9] Czinder B, Vásárhelyi B, Török Á. Long-term abrasion of rocks assessed by micro-Deval tests and estimation of the abrasion process of rock types based on strength parameters. Engineering Geology 2021;282:105996.

[10] Guo Y, Xie J, Fan Z, Markine V, Connolly DP, Jing G. Railway ballast material selection and evaluation: A review. Construction and Building Materials 2022;344:128218.

[11] Jia W, Markine V, Guo Y, Jing G. Experimental and numerical investigations on the shear behaviour of recycled railway ballast. Construction and Building Materials 2019;217:310–20. https://doi.org/10.1016/j.conbuildmat.2019.05.020.

[12] Qian Y, Boler H, Moaveni M, Tutumluer E, Hashash YM, Ghaboussi J. Characterizing ballast degradation through Los Angeles abrasion test and image analysis. Transportation Research Record 2014;2448:142–51.

[13] Qian Y, Boler H, Moaveni M, Tutumluer E, Hashash YM, Ghaboussi J. Degradation-related changes in ballast gradation and aggregate particle morphology. Journal of Geotechnical and Geoenvironmental Engineering 2017;143:04017032.

[14] Guo Y, Markine V, Song J, Jing G. Ballast degradation: Effect of particle size and shape using Los Angeles Abrasion test and image analysis. Construction and Building Materials 2018;169:414–24. https://doi.org/10.1016/j.conbuildmat.2018.02.170.

[15] Selig ET, Waters JM. Track geotechnology and substructure management. Thomas Telford; 1994.

[16] Guo Y, Zhao C, Markine V, Jing G, Zhai W. Calibration for discrete element modelling of railway ballast: A review. Transportation Geotechnics 2020;23:100341.

[17] Guo Y, Markine V, Zhang X, Qiang W, Jing G. Image analysis for morphology, rheology and degradation study of railway ballast: A review. Transportation Geotechnics 2019;18:173–211. https://doi.org/10.1016/j.trgeo.2018.12.001.

[18] Coetzee C, Nel R. Calibration of discrete element properties and the modelling of packed rock beds. Powder Technology 2014;264:332–42.

[19] Hossain Z, Indraratna B, Darve F, Thakur P. DEM analysis of angular ballast breakage under cyclic loading. Geomechanics and Geoengineering: An International Journal 2007;2:175–81.

[20] Ouhbi N, Voivret C, Perrin G, Roux J-N. Railway ballast: grain shape characterization to study its influence on the mechanical behaviour. Procedia Engineering 2016;143:1120–7.

[21] Tolomeo M, McDowell GR. Modelling real particle shape in DEM: a comparison of two methods with application to railway ballast. International Journal of Rock Mechanics and Mining Sciences 2022;159:105221. https://doi.org/10.1016/j.ijrmms.2022.105221.

[22] Tolomeo M, McDowell GR. DEM study of an “avatar” railway ballast with real particle shape, fabric and contact mechanics. Granular Matter 2023;25:32. https://doi.org/10.1007/s10035-023-01322-1.

[23] Govender N, Wilke DN, Kok S. Collision detection of convex polyhedra on the NVIDIA GPU architecture for the discrete element method. Applied Mathematics and Computation 2015;267:810–29. https://doi.org/10.1016/j.amc.2014.10.013.

[24] Azéma E, Estrada N, Radjaï F. Nonlinear effects of particle shape angularity in sheared granular media. Physical Review E 2012;86. https://doi.org/10.1103/PhysRevE.86.041301.

[25] Azéma E, Radjai F, Dubois F. Packings of irregular polyhedral particles: Strength, structure, and effects of angularity. Physical Review E 2013;87. https://doi.org/10.1103/PhysRevE.87.062203.

[26] Binaree T, Azéma E, Estrada N, Renouf M, Preechawuttipong I. Combined effects of contact friction and particle shape on strength properties and microstructure of sheared granular media. Physical Review E 2020;102. https://doi.org/10.1103/PhysRevE.102.022901.

[27] Azéma E, Radjaï F. Stress-strain behavior and geometrical properties of packings of elongated particles. Physical Review E 2010;81. https://doi.org/10.1103/PhysRevE.81.051304.

[28] Boton M, Azéma E, Estrada N, Radjaï F, Lizcano A. Quasistatic rheology and microstructural description of sheared granular materials composed of platy particles. Physical Review E 2013;87. https://doi.org/10.1103/PhysRevE.87.032206.

[29] Wiącek J, Molenda M. Effect of particle size distribution on micro- and macromechanical response of granular packings under compression. International Journal of Solids and Structures 2014;51:4189–95. https://doi.org/10.1016/j.ijsolstr.2014.06.029.

[30] Wiącek J, Molenda M. Numerical analysis of compression mechanics of highly polydisperse granular mixtures with different PSD-s. Granular Matter 2018;20. https://doi.org/10.1007/s10035-018-0788-z.

[31] Azéma E, Linero S, Estrada N, Lizcano A. Shear strength and microstructure of polydisperse packings: The effect of size span and shape of particle size distribution. Physical Review E 2017;96. https://doi.org/10.1103/PhysRevE.96.022902.

[32] Cantor D, Azéma E, Sornay P, Radjai F. Rheology and structure of polydisperse three-dimensional packings of spheres. Physical Review E 2018;98:052910. https://doi.org/10.1103/PhysRevE.98.052910.

[33] Cantor D, Azéma E, Preechawuttipong I. Microstructural analysis of sheared polydisperse polyhedral grains. Phys Rev E 2020;101:062901. https://doi.org/10.1103/PhysRevE.101.062901.

[34] Estrada N. Effects of grain size distribution on the packing fraction and shear strength of frictionless disk packings. Physical Review E 2016;94. https://doi.org/10.1103/PhysRevE.94.062903.

[35] Voivret C, Radjaï F, Delenne J-Y, El Youssoufi MS. Multiscale Force Networks in Highly Polydisperse Granular Media. Physical Review Letters 2009;102. https://doi.org/10.1103/PhysRevLett.102.178001.

[36] Nguyen D-H, Azéma E, Sornay P, Radjai F. Effects of shape and size polydispersity on strength properties of granular materials. Physical Review E 2015;91. https://doi.org/10.1103/PhysRevE.91.032203.

[37] Binaree T, Preechawuttipong I, Azéma E. Effects of particle shape mixture on strength and structure of sheared granular materials. Physical Review E 2019;100. https://doi.org/10.1103/PhysRevE.100.012904.

[38] Radjai F, Dubois F. Discrete-element modeling of granular materials. Wiley-ISTE. F. Radjai and F. Dubois; 2011.

[39] Saussine G, Cholet C, Gautier PE, Dubois F, Bohatier C, Moreau JJ. Modelling ballast behaviour under dynamic loading. Part 1: A 2D polygonal discrete element method approach. Computer Methods in Applied Mechanics and Engineering 2006;195:2841–59. https://doi.org/10.1016/j.cma.2005.07.006.

[40] Nader F, Pizette P, Govender N, Wilke DN, Ferellec J-F. Modelling realistic ballast shape to study the lateral pull behaviour using GPU computing. EPJ Web Conf 2021;249:06003. https://doi.org/10.1051/epjconf/202124906003.

[41] Jean M, Moreau JJ. Dynamics in the Presence of Unilateral Contacts and Dry Friction: A Numerical Approach. In: Piero G, Maceri F, editors. Unilateral Problems in Structural Analysis — 2, Vienna: Springer Vienna; 1987, p. 151–96. https://doi.org/10.1007/978-3-7091-2967-8_10.

[42] Sánchez P, Renouf M, Azéma E, Mozul R, Dubois F. A contact dynamics code implementation for the simulation of asteroid evolution and regolith in the asteroid environment. Icarus 2021;363:114441. https://doi.org/10.1016/j.icarus.2021.114441.

[43] Tafesse S, Robison Fernlund JM, Sun W, Bergholm F. Evaluation of image analysis methods used for quantification of particle angularity. Sedimentology 2013;60:1100–10. https://doi.org/10.1111/j.1365-3091.2012.01367.x.

[44] Mitchell JK, Soga K. Fundamentals of Soil Behavior. 3rd Edition. New York: May 2005; n.d.

[45] Kumara JJ, Hayano K. Deformation characteristics of fresh and fouled ballasts subjected to tamping maintenance. Soils and Foundations 2016;56:652–63.

[46] Indraratna B, Salim W. Deformation and degradation mechanics of recycled ballast stabilised with geosynthetics. Soils and Foundations 2003;43:35–46.

[47] Jean M. The non-smooth contact dynamics method. Computer Methods in Applied Mechanics and Engineering 1999;177:235–57. https://doi.org/10.1016/S0045-7825(98)00383-1.

[48] Radjai F, Richefeu V. Contact dynamics as a nonsmooth discrete element method. Mechanics of Materials 2009;41:715–28. https://doi.org/10.1016/j.mechmat.2009.01.028.

[49] Cundall PA, Strack ODL. A discrete numerical model for granular assemblies. Géotechnique 1979;29:47–65. https://doi.org/10.1680/geot.1979.29.1.47.

[50] Renouf M, Dubois F, Alart P. A parallel version of the non smooth contact dynamics algorithm applied to the simulation of granular media. Journal of Computational and Applied Mathematics 2004;168:375–82. https://doi.org/10.1016/j.cam.2003.05.019.

[51] https://git-xen.lmgc.univ-montp2.fr/lmgc90/lmgc90_user/.

[52] Azéma E, Radjaï F, Peyroux R, Saussine G. Force transmission in a packing of pentagonal particles. Physical Review E 2007;76:011301. https://doi.org/10.1103/PhysRevE.76.011301.

[53] Voivret C, Radjaï F, Delenne J-Y, El Youssoufi MS. Space-filling properties of polydisperse granular media. Physical Review E 2007;76. https://doi.org/10.1103/PhysRevE.76.021301.

[54] GDR MiDi. On dense granular flows. The European Physical Journal E 2004;14:341–65. https://doi.org/10.1140/epje/i2003-10153-0.

[55] Andreotti B, Forterre Y, Pouliquen O. Granular Media: Between Fluid and Solid. Cambridge: Cambridge University Press; 2013. https://doi.org/10.1017/CBO9781139541008.

[56] Cambou B, Jean M, Radjaï F, others. Micromechanics of granular materials. Wiley Online Library; 2009.

[57] Rothenburg L, Bathurst. Analytical Study of Induced Anisotropy in Idealized Granular Materials. Geotechnique 1989;39:601–14.

[58] Azéma E, Radjai F, Saussine G. Quasistatic rheology, force transmission and fabric properties of a packing of irregular polyhedral particles. Mechanics of Materials 2009;41:729–41. https://doi.org/10.1016/j.mechmat.2009.01.021.

[59] Quezada JC, Breul P, Saussine G, Radjai F. Penetration test in coarse granular material using Contact Dynamics Method. Computers and Geotechnics 2014;55:248–53. https://doi.org/10.1016/j.compgeo.2013.09.006.